Computers in Biology and Medicine 161 (2023) 107019

Contents lists available at ScienceDirect

Computers in Biology and Medicine

journal homepage: www.elsevier.com/locate/compbiomed

Spatiotemporal estimations of temperature rise during electroporation treatments using a deep neural network

Edward J. Jacobs IV [a,*], Sabrina N. Campelo [a], Kenneth N. Aycock [a], Danfeng Yao [b], Rafael V. Davalos [a]

[a] Department of Biomedical Engineering and Mechanics, Virginia Tech-Wake Forest University, Blacksburg, VA, USA
[b] Department of Computer Science, Virginia Tech, Blacksburg, VA, USA

ARTICLE INFO

Keywords:
Electroporation
Thermal heating
Artificial intelligence
Pulsed electric field
Tissue ablations

ABSTRACT

The nonthermal mechanism for irreversible electroporation has been paramount for treating tumors and cardiac tissue in anatomically sensitive areas, where there is concern about damage to nearby bowels, ducts, blood vessels, or nerves. However, Joule heating still occurs as a secondary effect of applying current through a resistive tissue and must be minimized to maintain the benefits of electroporation at high voltages. Numerous thermal mitigation protocols have been proposed to minimize temperature rise, but intraoperative temperature monitoring is still needed. We show that an accurate and robust temperature prediction AI model can be developed using estimated tissue properties (bulk and dynamic conductivity), known geometric properties (probe spacing), and easily measurable treatment parameters (applied voltage, current, and pulse number). We develop the 2-layer neural network on realistic 2D finite element model simulations with conditions encompassing most electroporation applications. Calculating feature contributions, we found that temperature prediction is mostly dependent on current and pulse number and show that the model remains accurate when incorrect tissue properties are intentionally used as input parameters. Lastly, we show that the model can predict temperature rise within ex vivo perfused porcine livers, with error <0.5 °C. This model, using easily acquired parameters, is shown to predict temperature rise in over 1000 unique test conditions with <1 °C error and no observable outliers. We believe the use of simple, readily available input parameters would allow this model to be incorporated in many already available electroporation systems for real-time temperature estimations.

1. Introduction

Irreversible electroporation (IRE) is a nonthermal focal ablation modality that employs high-magnitude (1–3 kV), short (70–100 μs) electric pulses applied directly into tissue [1]. The resulting electric field generates a transmembrane potential (TMP) on cells to overcome the forces holding the phospholipid bilayer together and achieve a dielectric breakdown of the membrane. Electroporation theory and experiments show that nanoscale pores form when induced TMP values exceed a critical threshold (~0.2–1 V) [2] [-] [6], allowing for the flow of current across the membrane. The transitory formation of pores is called reversible electroporation and has been used to successfully deliver chemotherapeutics [7] [-] [9], genes [10,11], and substances that would otherwise be impermeable into the cell. With the application of larger and longer potentials, cells are unable to maintain homeostasis and die through necrosis or apoptosis. This is termed irreversible electroporation (IRE) and is used to generate clinically relevant ablations without the need for chemotherapeutics and without significant thermal heating [12–14]. IRE is being used clinically to treat tumors situated near sensitive structures, where surgical resection and thermal ablation methods are contraindicated; this includes locally advanced and unresectable liver [15–17], kidney [18], prostate [19,20], and pancreatic [21] malignancies. Furthermore, IRE is being investigated as an alternative cardiac ablation modality in the treatment of atrial and ventricular fibrillation [22].

IRE has the advantage of ablations formation being independent of thermal effects, which is paramount for treating tumors in anatomically sensitive areas where there is concern about damage to nearby bowels [23], ducts [24], blood vessels [25], or nerves [26]. Further, IRE does not suffer from the heat sink effect seen in other ablation modalities, which may allow bulk tumor around blood vessels to survive treatment. However, Joule heating still occurs as a secondary effect of applying a

* Corresponding author. 325 Stanger St, Blacksburg, VA, 24061, USA.
E-mail address: edwja97@vt.edu (E.J. Jacobs).

https://doi.org/10.1016/j.compbiomed.2023.107019
Received 23 January 2023; Received in revised form 14 April 2023; Accepted 5 May 2023
Available online 16 May 2023

current through a resistive tissue and must be minimized to maintain these benefits, especially at high voltages. The administration and protocol for IRE treatments can generate varying degrees of thermal damage, which correlate to reported complications [27,28]. A recent systematic review estimated that 30% of the IRE-treatment region experiences mild-hyperthermic temperatures (40–50 °C) with ~5% being exposed to temperatures >50 °C [29]. Thermal heating is the main limiting factor in achieving larger ablations clinically; however, ablation size and temperature rise are both multifaceted and influenced by applied energy (voltage, pulses, pulse width), the rate the energy is applied (repetition rate), and tissue properties, which vary between patients and may be unknown for tumors. Further, existing clinical electroporation protocols do not actively consider thermal heating during IRE procedures, and generating larger ablation volumes is often at the expense of increased thermal damage [30].

Numerous thermal mitigation (TM) protocols have been proposed to minimize temperature rise. Innovative probe designs that incorporate heat-dissipating technologies such as phase-change materials or active cooling and pulse paradigm adjustments (that facilitate tissue perfusion to disperse heat between subsequent pulses) have been shown to reduce thermal damage [31–33]. The benefits of these techniques, however, must be evaluated against the added time, money, and effort needed to modify probes [34,35]. These methods only remove heat at the electrode surface and do not eliminate thermal effects altogether. Computer modeling is often used to prospectively and retrospectively simulate temperature rises during treatment, but without the addition of invasive sensing devices, real-time temperature monitoring is limited. Further, finite element modeling requires *a priori* knowledge about the system that may vary significantly from reality; the resulting current from an applied potential may be different during treatment than is simulated, making the prospective simulations imprecise. A recent study integrated Fourier Analysis SpecTroscopy (FAST), an approach for obtaining bioimpedance measurements during electroporation-based therapies, to predict temperature increases from the application of an electric field in agar phantoms [36,37]. However, FAST technologies are not commonly integrated in pulsing generators, making it difficult to extract diagnostic bioimpedance measurements in real time. Therefore, without real-time temperature monitoring during electroporation treatments, there is risk of undesired thermal damage since the amount of excessive thermal heating can significantly differ from developed models.

Here, we propose a 2-layer neural network (NN) to accurately monitor spatiotemporal temperature rise during pulsed electric field treatments, utilizing estimated tissue properties (bulk and dynamic conductivity), known geometric properties (probe spacing and exposure), and measurable treatment parameters (applied voltage, current, and pulse number). We train the NN on realistic COMSOL™ Multiphysics simulations with conditions encompassing most clinically relevant electroporation applications and show that it converges to an accurate solution (<1 °C) in the training, validation, and test datasets. Using feature contribution analysis, we found that temperature prediction is mostly dependent on current and pulse number and show that the model still predicts accurately even when incorrectly estimated tissue properties are intentionally used as input parameters. Lastly, we show that the model can accurately predict temperature rise within ex vivo perfused porcine livers, with error <0.5 °C between the predicted temperature and the recorded temperature. This model, using easily acquired parameters, is shown to predict accurate temperature rise in over 1000 conditions with no observable outliers and can be extrapolated to conditions it has not seen through pattern recognition. The use of NNs can overcome the limitations of finite element models, since they can predict the temperature rise as current is being read during treatment. Further, the use of simple and readily available input parameters would allow this model to be easily incorporated in many already available electroporation systems.

2. Materials and methods

2.1. Creating a finite element model (FEM) for temperature and current simulations

The goal of the finite element model (FEM) was to generate the dataset for supervised learning of a deep NN. The two values obtained from the FEM were the (1) applied current and (2) temperature rise within the domain over 200 pulses (Fig. 1A). Parameters that are known prior to treatment are electrode exposure, electrode spacing, voltage, and tissue property estimations; the applied current and temperature rise are unknown (Fig. 1B). We swept through 960 unique tissue, voltages, and geometric conditions, then calculated the resulting applied current and temperature distribution at every pulse number (Fig. 1C). The simulated current, pulse number, voltage, tissue parameters, and geometric conditions were used as the input for a 2-layer NN and trained using supervised learning against the simulated temperature. The output of the neural network is predicted spatiotemporal temperature rise at 20 locations between and around the electrodes (Fig. 1D).

To generate the dataset which the AI model is trained on, a two-dimensional FEM was employed in COMSOL™ Multiphysics 6.0 (COMSOL, Stockholm, Sweden) to simulate realistic tissue heating during electroporation treatments.

The tissue was modeled as an ellipse of dimensions 10 cm × 5 cm, with an out of plane thickness of 1 m. Two stainless steel electrodes were modeled as circles with radius, r_e. Both the center-to-center distance, D, and applied electric potential, Φ, between the electrodes were varied to develop 960 unique simulations to train the AI on. The electric potential at the end of an IRE pulse was calculated with a modified Laplace equation under the electro-quasistatic approximation:

$$-\nabla \bullet \left(\sigma\left(\left|\vec{E}\right|, \mathrm{T}\right)\nabla\Phi\right) = 0 \tag{1}$$

where the electrical conductivity, σ, is a function of both temperature, T, and electric field magnitude, $\left|\vec{E}\right|$. The boundary of the electrodes in contact with the tissue was set to $\Phi = \mathrm{V}$ and $\Phi = 0$, for the source and sink, respectively. The outer boundary of the tissue was treated as electrically insulated. The resulting electric field was calculated as:

$$\vec{E} = -\nabla\Phi \tag{2}$$

Prior studies have shown that the tissue conductivity is a function of the applied electric field magnitude. As the tissue transitions from an non-electroporated state to a fully electroporated state, the tissue conductivity tends to increase and plateau [38]. This dynamic conductivity is solved in the steady state solution and can be modeled as:

$$\sigma\left(\left|\vec{E}\right|\right) = \sigma_o + \frac{M}{1 + De^{\frac{-\left|\vec{E}\right|-A}{B}}} \tag{3}$$

where σ_o is the baseline tissue conductivity and M is the increase in conductivity due to electroporation. Both of these values were varied within the COMSOL model. $\left|\vec{E}\right|$ is the magnitude of the electric field, A = 580 V/cm, B = 120 V/cm, and D = 10 are empirically determined sigmoidal function parameters; further, we chose to only vary σ_o and M, because they have the most impact on heating and resulting current [27].

Tissue temperature was computed using the Pennes' bioheat equation with the addition of Joule heating from the applied electric field (eq (4), middle term):

$$c_{p,t}\rho_t\frac{\partial T}{\partial t} = \nabla \bullet (k_t\nabla\mathrm{T}) + \sigma_t(T)\left|\nabla\vec{E}\right|^2 \bullet \frac{pw}{\tau} + c_{p,b}\rho_b\omega_t(T_0 - T) \tag{4}$$

where $c_{p,t}$ is the tissue specific heat, ρ_t is the tissue density, k_t is the tissue thermal conductivity, and σ_t is the tissue electrical conductivity. pw is

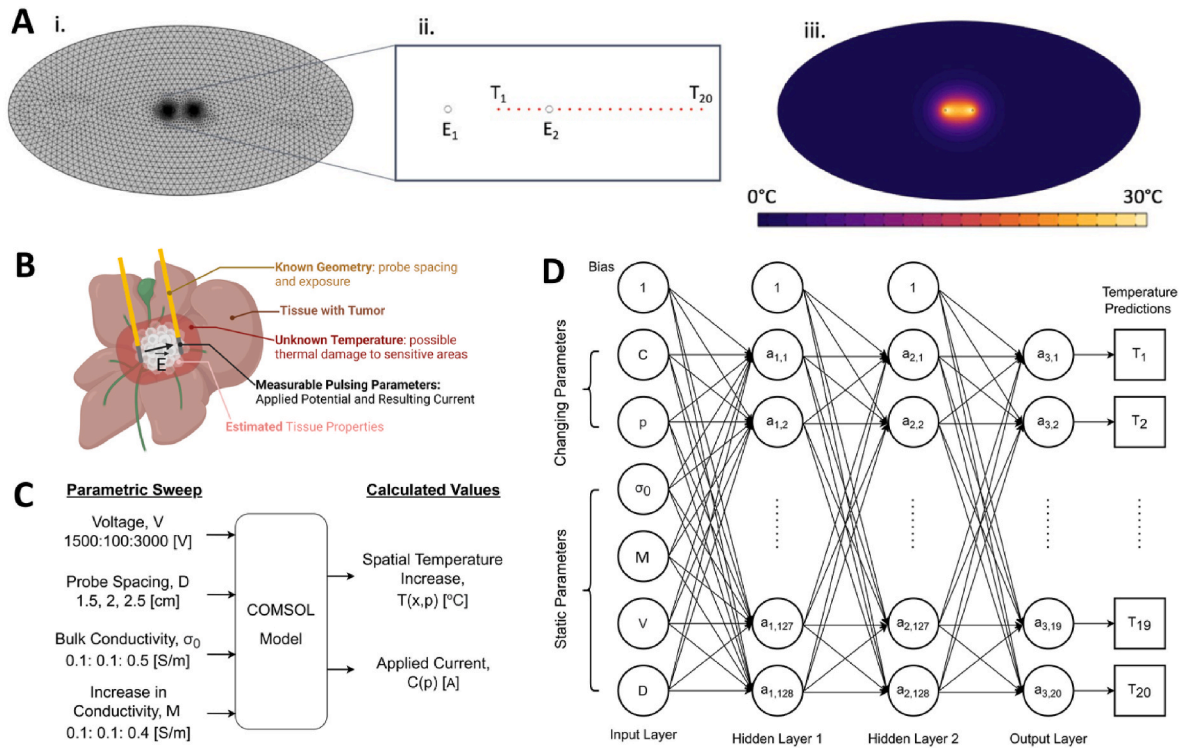

Fig. 1. Creating the Model. **A) i.** COMSOL™ Multiphysics 6.0 was used to simulate temperature rise during IRE treatments within a 2D tissue domain. **ii.** Temperature was sampled at 20 different points (x) between and outside of the two electrodes (E_1 & E_2). **iii.** Representative image of the temperature distribution within the simulation. **B)** The information known during electroporation treatments are the probe geometry, the pulsing parameters, and the estimated tissue properties. The current and pulse number are measurable parameters during treatment. Temperature distributions are unknown. **C)** A parametric sweep for multiple conditions of voltage, probe spacing, bulk tissue conductivity, and increase in tissue conductivity due to the electric field were simulated to generate 960 unique models. Current measurements were then calculated each pulse (p), and temperature values were measured every position (x) for each pulse. **D)** The temperature prediction model is a 2-layer fully-connected perceptron. Both hidden layers have a Rectified Linear Unit (ReLU) activation function, and the output layer has a linear activation function. The input layer has 6 nodes for each feature, both hidden layers have 128 nodes, and the output layer has 20 nodes for each temperature position (x). The loss function was defined as mean-squared error (MSE) and trained with ADAM to calculate the entropy between the 20 predicted temperature points and the 20 simulated COMSOL temperatures.

the pulse width for the IRE pulse and τ is the period of the pulse. For this study we chose to model a pulse width of 100 μs and a period of 1 s, because that is what is commonly used for cancer ablation applications. The ratio of the two is the duty cycle, which is proportional to the heat generated within the tissue. Temperature is also removed from the tissue through blood perfusion, where $c_{p,b}$ is the specific heat of blood, ρ_b is the density of blood, ω_t is the tissue perfusion rate, and T_0 is the temperature of perfused blood, 37 °C [39]. The values used within the FEM models and their references are given in Table 1.

The conductivity of tissue also changes with temperature. To accurately predict the electric field within the tissue, we update the solution for the steady state conductivity:

$$\sigma_t(T) = \sigma \bullet (1 + \alpha \bullet (T - T_0)) \tag{5}$$

where α is the thermal coefficient of conductivity; as the temperature increases, the conductivity will also increase [40,41]. The 2D COMSOL model was run using an extra fine mesh size (the highest mesh) with 10, 702 domain elements and 216 boundary elements. The default solver configurations in COMSOL were used for the stationary and time-dependent solver. Three edits were made to the stationary solver: (1) The relative tolerance was changed from 0.001 to 0.0001, (2) solving method was switched from automatic to automatic highly nonlinear, and (3) the maximum number of iterations was increased from 25 to 250. In the time-dependent solver, the time stepping was switched from free to intermediate. All these changes were done to increase the accuracy and reproducibility of the COMSOL model.

A 2D model was chosen over a 3D model to minimize the computational burden needed to create the dataset. We verified that the two values calculated from the FEM, current and temperature distribution, were not significantly different between 2D and 3D. We reconstructed a representative model of the liver using 3D Slicer v5.2 and

Table 1
Parameters for the COMSOL™ multiphysics model.

Parameters	Symbol	Value(s)	Reference
Bulk Tissue Conductivity	σ_o [S•m^{-1}]	0.1, 0.2, 0.3, 0.4, 0.5	Varied
Increase in Electroporated Tissue Conductivity	M [S•m^{-1}]	0.1, 0.2, 0.3, 0.4	Varied
Tissue Density	ρ_t [kg•m^{-3}]	1050	[15]
Tissue Heat Capacity	$c_{p,t}$ [J•kg^{-1} K^{-1}]	3886	[15]
Tissue Thermal Conductivity	k_t [W•m^{-1} K^{-1}]	0.50	[15]
Temperature-Dependent Conductivity Change	α [%•K^{-1}]	0.015	[16]
Electrode Radius	r_e [mm]	0.5	Measured
Applied Voltage	**V** [V]	1500-3000; 100V interval	Varied
Pulse Width	**pw** [μs]	100	Set Here
Pulse Period	τ [s]	1	Set Here
Initial Temperature	T_o [°C]	37	Measured
Center-to-center Probe Spacing	**D** [cm]	1.5, 2, 2.5	Varied
Tissue Blood Perfusion	ω_t [s^{-1}]	1.7 E−3	[42]
Blood Density	ρ_b [kg•m^{-3}]	1050	[42]
Blood Specific Heat	$c_{p,b}$ [J•kg^{-1}•K^{-1}]	3617	[42]

imported the 3D model into COMSOL (Fig. 2A). We found that the temperature distributions were not significantly different between the 2D and 3D models (Fig. 2B). We measured the temperature at the 20 locations used for the NN and found that the temperature was the same between the 2D and 3D model, with an R^2 value of 0.9936 (Fig. 2C). Further, we measured the applied current for 3 electrode exposures (1.5, 2, and 3 cm) at all the applied voltages (1500–3000 V; 100 V interval) used for the 2D model (Fig. 2D). The applied current in the 3D model is simply the applied current in the 2D model, scaled by the electrode exposure (Fig. 2E&F). This allows us to scale measured currents by the electrode exposure for use within the NN, without having to explicitly define electrode exposure in the FEM parameters or NN inputs.

2.2. Creating an input and output dataset for a multi-layer perceptron

We varied the geometric (center-to-center probe spacing, *D*), tissue parameters (bulk conductivity, σ_o, and increase in electroporated tissue conductivity, *M*), and treatment parameters (applied voltage, *V*) as specified in Table 1. These values were used as the input parameters for the finite element model (Fig. 1C). The time-dependent solution simulated a treatment from pulse 1 to 200. The current was calculated by integrating the current density across the perimeter of the source electrode, then multiplying by the probe exposure, which was assumed to be 2 cm. We chose to measure the temperature at 5 locations between and 15 locations outside the electrodes as shown in Fig. 1A. The temperature distribution is symmetric, where position 0 is at the midpoint between the two probes. Position 5 is located at the probe center and is not recorded for this reason. The physical locations of the 20 temperature points are different for each probe spacing. Therefore, we normalized the real locations for temperature reading in COMSOL by the known center-to-center probe spacing with:

$$position = 10 * \frac{location}{probe\ spacing} \tag{6}$$

to get 20 nondimensional positions. The inverse of this equation can translate AI-predicted temperatures at the dimensionless positions to real locations. The physical locations are labeled 1–20. After normalizing, the positions are given by 0–20, skipping 5 at the electrode location. Normalized positions are used for all the analyses.

Each specific condition and pulse number is treated as its own isolated data point and is unique from any other row in the dataset. The current derived at that pulse number for that specific condition was added to the input for that condition to create the input dataset. The simulated temperature at all 20 locations was matched to the corresponding row in the input dataset to the create the output dataset. These two datasets constitute the whole dataset. 5% of this was set aside as the

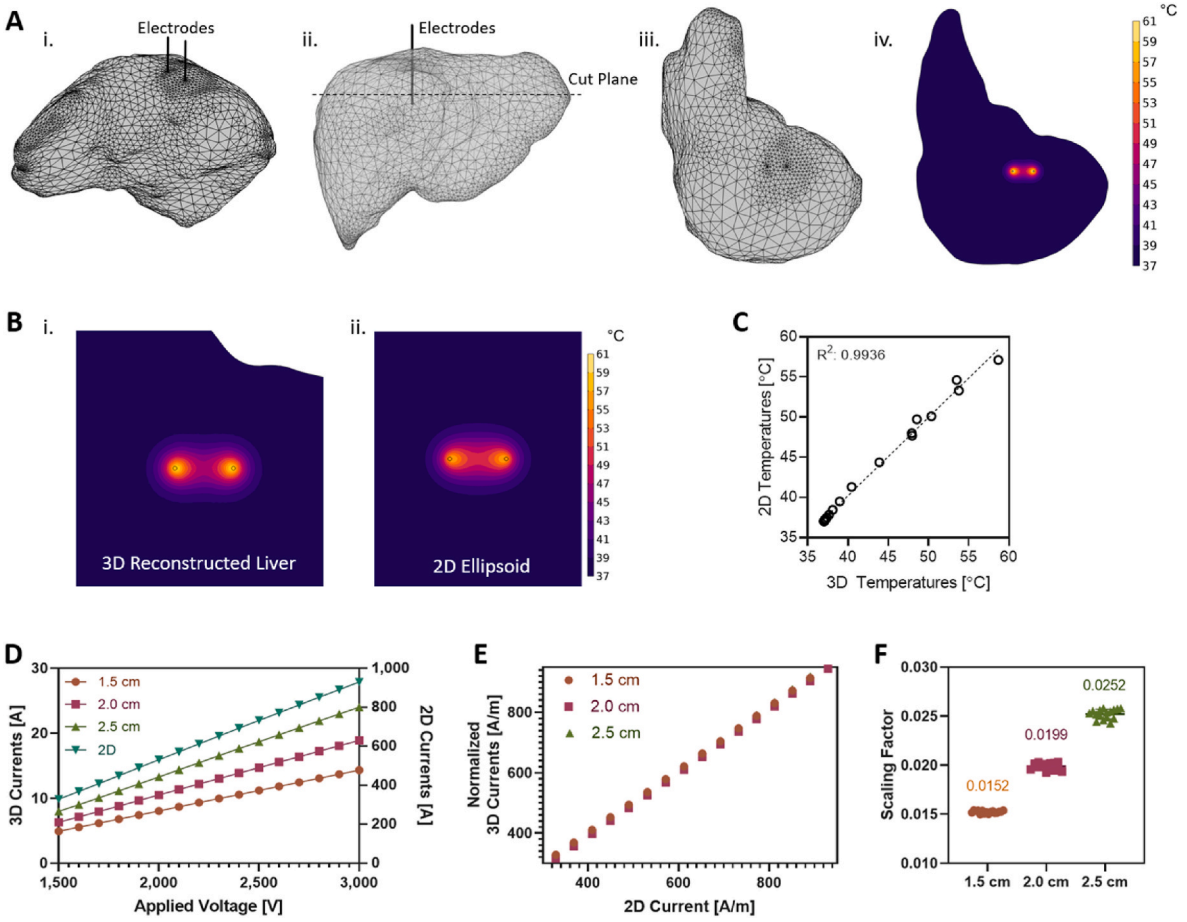

Fig. 2. Comparison between 3D reconstructed liver and 2D simplification. A) (i.) A human liver scan was reconstructed using 3D Slicer and imported into COMSOL with an inserted 2-needle probe geometry (1.5-cm spacing) matching geometry used with the 2D models. (ii.) Transparent side view and (iii.) top-down view shows the needle insertion within the liver. A cut plane was defined through the center of the electrode exposure. (iv.) Temperature distribution plotted on the 2D cut plane. B) Zoomed in temperature distributions for the (i.) 3D reconstructed liver and (ii.) the simplified 2D ellipsoid show minimal variation in heating at pulse 100. C) Linear regression of the spatial temperature locations between the 3D reconstructed liver and the 2D approximation. D) COMSOL simulated currents for the 2D model (right axis) and three 3D models with different electrode exposures (left axis). Both models have the same tissue properties. E) Normalizing the 3D model currents by dividing by the exposure length (0.015, 0.02, and 0.025 m) F) Scaling factor for each electrode exposure is simply the electrode exposure. The current for each 3D model was divided by the current from the 2D model at each applied voltage.

test dataset and not used for training. We chose 5% since that corresponds to ~2000 test datapoints. We calculated a minimum 345 samples needed using the 95% confidence interval on our results. This constitute ~6x the required size; however, less than 5% of the total dataset was not used to reduce sampling bias. The validation dataset was defined during training using 10-fold cross validation and shuffled each training epoch.

2.3. Creating and training a two-layer perceptron for spatial temperature prediction

A deep neural network (NN) with two hidden layers was defined and trained within Google Colab (Alphabet) using the Keras python interface for the TensorFlow library (Fig. 1D). The first hidden layer was defined as a dense layer with 128 neurons and 6 inputs for each feature in the input dataset. The second layer was also defined with 128 neurons. Both hidden layers were defined to have the rectified linear activation function (ReLu). The output layer was defined as a dense layer with 20 neurons and a linear activation function. The MLP was trained using the mean-squared error loss function and Adam optimizer over 50 epochs. A validation split was set at 10% and shuffled every epoch. Mean absolute error was set as a metric to be calculated for each epoch during training. The model was finalized to have 19,988 total trainable parameters.

2.4. Ex vivo machine perfused porcine liver

Clinically representative two-needle IRE treatments were performed in a validated perfused organ model [43] as previously described to generate experimental temperature and current data [31,33]. Briefly, porcine livers were excised at a local abattoir within 15 min of euthanasia, fitted with Luer-lock connectors, and immediately flushed at constant pressure (~90 mmHg) with 4 L of modified phosphate buffered saline. Livers were transported via static cold storage for ~90 min prior to being briefly flushed and anastomosed to a machine perfused organ preservation system. Perfusate temperature was set to and maintained at 30 °C throughout the experiment.

IRE treatment consisted of a total of 90 pulses (1600 V) with 90 μs duration, delivered at a rate of 1.5 Hz with a custom generator (VoltMed Inc., Blacksburg, VA). After each set of 10 pulses, a 3.5 s delay was observed to simulate the pulse delivery strategy of the NanoKnife® system (the delay is used to recharge capacitors). NanoKnife® (Angio-Dynamics, Inc., Latham, NY) electrodes (Ø = 1 mm) with 1.5-cm exposure were used for the experiments, and a custom holder was used to maintain 1 cm parallel spacing. Treatment voltage and current were monitored with a high-voltage probe (Enhancer 3000, Harvard Bioscience, Holliston, MA) and passive current probe (Pearson Electronics, Palo Alto, CA), respectively, each of which were connected to an oscilloscope (3024z, Teledyne LeCroy, Chestnut Ridge, NY). The oscilloscope was triggered on the rising edge of each IRE pulse, and the corresponding voltage and current waveforms were saved to individual files with ~10 ns resolution. For comparison to the MLP, voltage and current data were extracted by averaging the recorded values during the last 10 μs of each individual pulse.

To record intraoperative temperature, two fiber optic temperature (FOT) sensors (Advanced Energy, Santa Clara, CA) were placed within the treatment zone. One FOT was affixed to the needle electrode surface at the midpoint of the exposure, while the other was inserted into the center of the tissue between the two electrodes. After calibration of the FOT probes, temperature was recorded at both sites at a rate of 2 Hz.

2.5. Statistical analysis

All data analysis and statistics were performed in Prism 9.0 (GraphPad) with an $\alpha = 0.05$.

3. Results

3.1. The model training and validation error converges to <1 °C error

The deep neural network (NN) was trained for 50 epochs using the ADAM optimizer to minimize the mean-squared error (MSE) loss function. The model error quickly converged within 10 epochs and plateaued before the end of training at 50 epochs. The validation dataset and training dataset did not diverge, suggesting the model was not overfit (Fig. 3A). MSE values do not offer insight to how accurate the model is, so a metric of mean absolute error (MAE) was calculated after each epoch. The MAE on the output of this model is the mean of the absolute differences between AI predicted temperature and COMSOL simulated temperature. The MAE for predictions from the training and validation dataset were 0.91 °C and 0.94 °C, respectively (Fig. 3B). The 5% test data was run through the trained model and had a MAE of 0.89 °C. This suggests the model can translate the relationship found between the input and output data within the training set to input data it has never seen.

To demonstrate that we can accurately predict the temperature distributions with a two-probe set up and that the solutions converged during training, we randomly initialized the AI model, trained it, and predicted the temperature distribution using the input conditions five times. We plot the change in temperature for all 20 positions using two randomly chosen conditions within the test dataset (Fig. 3C). The two conditions are summarized in Table 2. Since one of our input parameters is center-to-center probe separation and the MLP requires a constant number of outputs (20), we normalized the 20 real temperature locations by the probe separation to give 20 normalized positions (see methods), which can also be translated back into real locations. Fig. 3C shows that the model converges to an accurate solution every time it is trained, with a small standard deviation for the temperature prediction. Subsequently, there is not a significant difference between the AI predicted temperature rise and the COMSOL simulated temperature rise. The R-squared values for the linear regression between the AI predicted temperature rise and COMSOL simulated temperature rise are 0.95 and 0.997 for conditions 1 and 2, respectively.

3.2. The trained model can accurately predict temperature distributions on the test data

The results for the test dataset error between the AI predicted temperature rise and the COMSOL simulated temperature rise are given in Fig. 4. The test dataset is 5% of the total dataset that was set aside prior to training and consists of 1968 unique conditions. None of the conditions within the test dataset were present in the training set, so the AI has never seen these unique parameters. From the linear regression through the AI simulated temperature versus the COMSOL simulated temperature (Fig. 4A), we show that the predictions and simulations are strongly correlated. Further, there are no noticeable outliers from the regression. Every regression is strongly correlated with R-squared values above 0.9 at each position. Positions 0–10 had the highest R-squared values above 0.99, and subsequently were the positions with the greatest temperature rise due to their proximity to the electrodes. This also explains why these locations had the most relative error (Fig. 4B) and absolute error (Fig. 4C). From position 10 to position 20, there is a sharp decrease in overall temperature rise with a corresponding decrease in R-squared values. Both the average error and average absolute error were under 2 °C for every position, with the most error being between positions 0 and 7. Further, the 95% confidence interval for the error encompassed 0 for every temperature position (Fig. 4B), suggesting there is not a significant difference between the AI predicted temperature and the COMSOL predicted temperature.

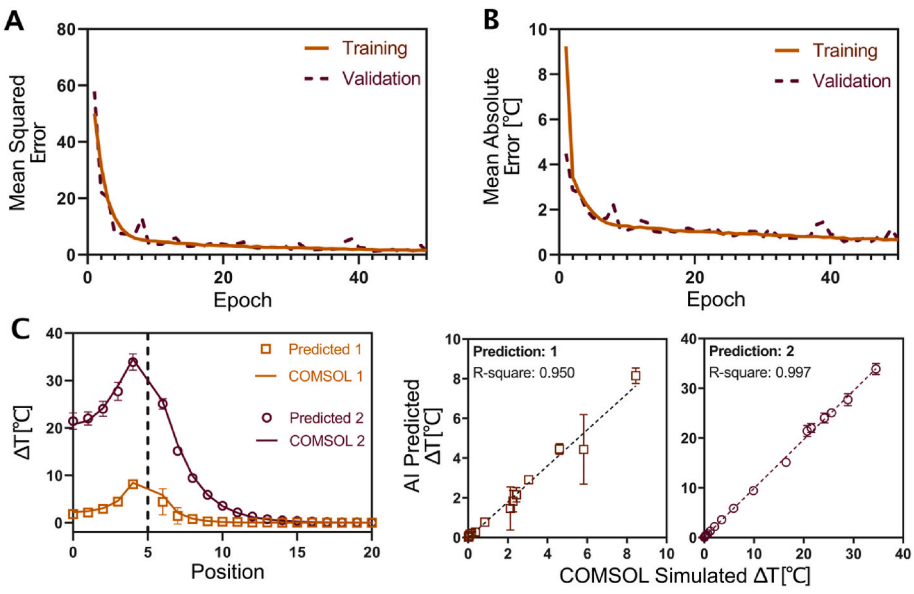

Fig. 3. Training Results. **A)** The training and validation error over 50 epochs show convergence of the loss function. **B)** The mean absolute error was calculated as a metric at the end of each epoch for the training and validation dataset. **C)** AI predicted and COMSOL simulated temperatures from 2 randomly selected conditions in the test data set. The AI was cleared, randomly initialized, and trained 5 times; each data point is the mean and std. of the predictions across the different trainings. Linear regressions for the COMSOL simulated increase in temperature versus the AI predicted increase in temperature show a good prediction of the AI on data it has not been explicitly trained on.

Table 2
Random conditions used for comparison.

Condition	D [cm]	V [V]	σ_0 [S/m]	M [S/m]	Pulse [n]	Current
1	2	2100	0.5	0.3	145	24.566
2	2.5	2500	0.4	0.2	10	27.815

3.3. Current measurements have the most influence on temperature distribution

To understand which input parameters have the most influence on the change in temperature, we performed feature contribution analysis with the SHapley Additive exPlanations (SHAP) library within Python. SHAP functions through cooperative game theory to find the importance of an input feature on the output metric [44–46]. SHAP values were calculated for each input parameter to the MLP (Fig. 5A). Current had the most influence on the output of the model, followed by pulse number and bulk conductivity. The change in conductivity due to electroporation had the lowest influence on the temperature output. The SHAP values for the neural network suggest that the tissue properties do not have a substantial contribution in predicting the rise in temperature.

Therefore, we wanted to know if measurable quantities (i.e, current) could compensate for incorrect estimates of tissue properties (i.e., conductivity). COMSOL models were run with three real parameters (Fig. 5B–E), and the current and spatial temperature values were found at pulse 100. This constitutes the real simulated physics of the tissue. The inputs to the trained AI, however, were edited, so that the tissue property inputs were incorrect, but the correct physical parameters (voltage, probe spacing, pulse number, and current) were used. The tissue properties (bulk conductivity or final conductivity) were either overestimated, underestimated, or correctly estimated. We show that despite having appreciably different estimations of both tissue properties, the predicted AI temperature was not significantly different from the COMSOL simulated temperatures (Fig. 5C&E).

3.4. The trained neural network can accurately predict temperature rise in an ex vivo organ model

To validate that our model can accurately predict temperature rise within real tissue, we used a perfused ex vivo porcine liver. Two probes with a 1.5 cm exposure were positioned 1 cm apart (a probe spacing the neural network was not explicitly trained on). A potential of 1600 V was applied in a train of 90 pulses at 1.5 Hz with 3.5 s delays after every 10 pulses. Applied voltage and current were monitored and recorded over the 90 pulses. Further, we recorded the temperature at two key points using a fiber optic temperature probe: the center between the two electrodes and at the electrode surface. The AI was trained with data from 2D COMSOL simulations, where the probe exposure is not explicitly defined. In training the AI, we multiplied the derived current by a scaling factor of 0.02 to represent a 2 cm exposure. We calculated scaling factors for different exposures (Fig. 2D) and see that we can multiply by the exposure length to scale the current from 2D to 3D. Subsequently, since the current is linearly dependent on the exposure, we multiplied the recorded currents by 0.75 to translate the current recorded with a 2 cm exposure to a 1.5 cm exposure to get the input to the model. The estimated tissue properties for the liver were 0.12 S/m for bulk conductivity and 0.3 S/m for the conductivity change due to electroporation effects, based on previous findings [31].

We see the neural network can accurately predict the real temperature rise in both 3D perfused livers (Fig. 6A and B). A linear regression of the AI predicted change in temperature versus the real recorded change in temperature shows a good fit with R-squared values above 0.98 for both livers and both temperature locations (Fig. 6C and D). The slope for the temperatures recorded at the probe were 1.04 and 1.03 showing that the AI did not over or under predict the temperatures. However, the slopes of the linear regressions for the temperatures at the center point were 0.82 and 0.88 for liver 1 and liver 2, respectively. This suggests that the AI slightly underpredicted the real temperature. Fig. 6E shows the error between the predicted change in temperature and the real change in temperature. We see for liver 1, the AI underpredicts the temperature rises by < 0.5 °C at both recorded positions. The 95% confidence interval for the error is given for each condition, and each confidence interval encompasses 0. This suggests that there is not a statistically significant error between the AI predicted temperature rise and the real recorded temperature rise. Further, the average of the absolute difference between the predicted and real temperatures are <0.6 °C for both positions in both livers (Fig. 6F).

4. Discussion

In this study, we have shown that an accurate and robust temperature prediction model can be developed using easily obtainable and available information: estimated tissue properties (bulk and dynamic conductivity), known geometric properties (probe spacing and

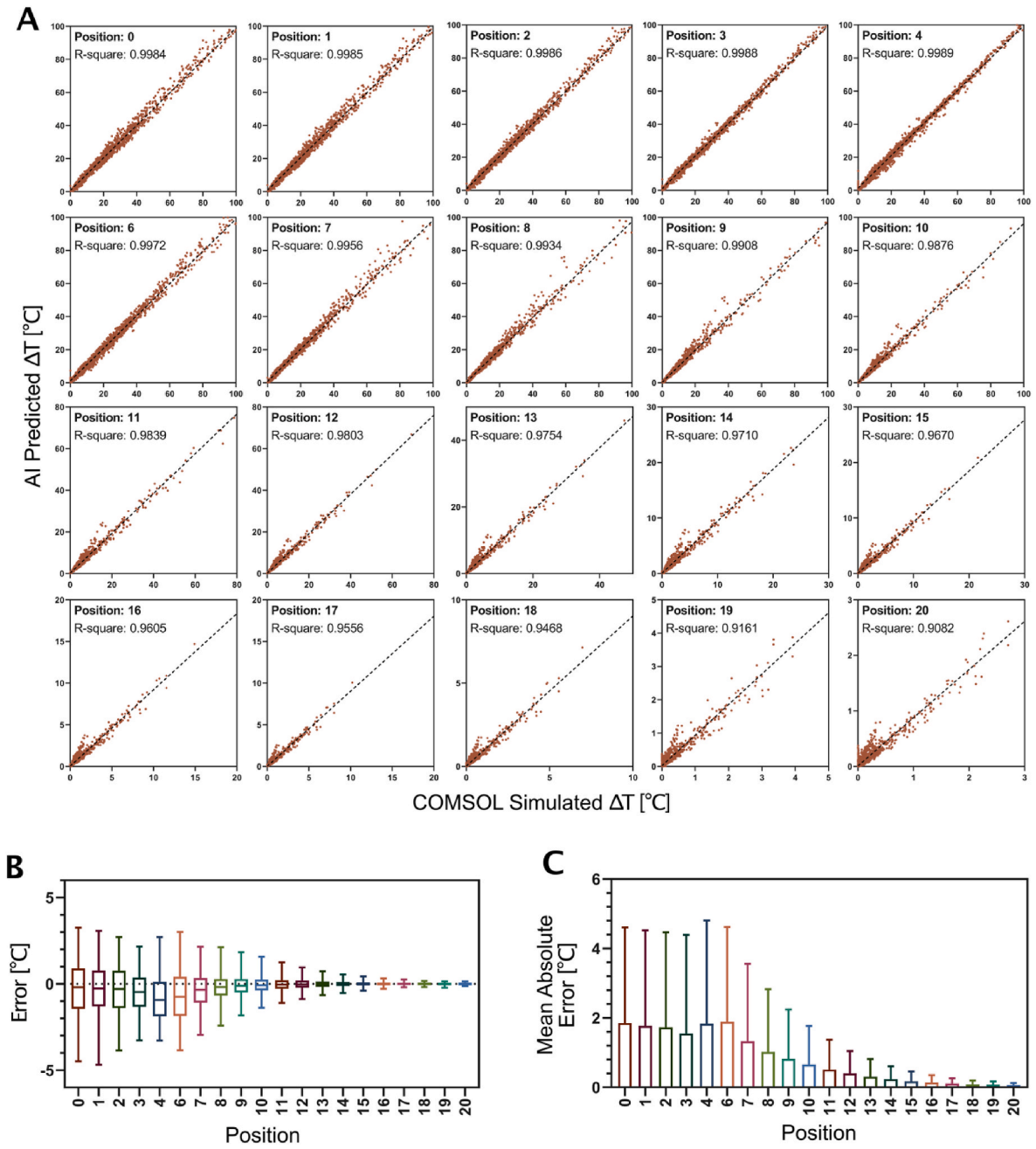

Fig. 4. Error between the AI predicted temperatures and the COMSOL simulated temperatures in the test data set. **A)** COMSOL simulated temperatures versus AI simulated temperature. Each subplot consists of 1968 conditions for that respective point from the test set. For positions 11–20, the axes were scaled because of the significant decrease in overall temperature rise away from the electrodes. **B)** Calculated error for each position is presented as a box plot with the 50% (box) and 99% (whisker) data ranges. **C)** Absolute error for each position is given as mean ± std.

exposure), and easily measurable treatment parameters (applied voltage, current, and pulse number). We show that the predictions converge to an accurate solution (<1 °C) in the training, validation, and test datasets, and further demonstrate that the trained model can accurately predict temperature rise at two locations in two ex vivo perfused porcine livers treated with IRE.

To minimize the time to run the COMSOL simulations, we chose to train the AI on data derived from a 2-dimensional COMSOL model. However, we show that the AI can still accurately predict the temperature rise in an ex vivo perfused organ model, with <0.5 °C error for both livers at both positions. While a 3D model would allow for the addition of electrode exposure as an input, we have verified that by scaling the current by the electrode exposure, we still achieve accurate current outputs comparable to those reported in 3D simulations.

In this model we chose to predict temperature at 20 locations such that there would be five locations between the electrodes, five in the transition region outside the electrodes, and ten tapering off to minimal temperature rise. Both the number and spacing of these locations can be changed when generating new datasets in COMSOL. Fig. 4 shows that both the error and temperature are near to zero by position 20, with mean simulated temperature rise <0.05 °C. This encompasses any points of interest for investigating temperature rise. Further, we chose not to normalize the temperature outputs during training, so the positions with the most temperature rise would also have the most error. Thus, the training optimization was forced to focus on these points. This is seen with the higher temperature positions having larger R-squared values

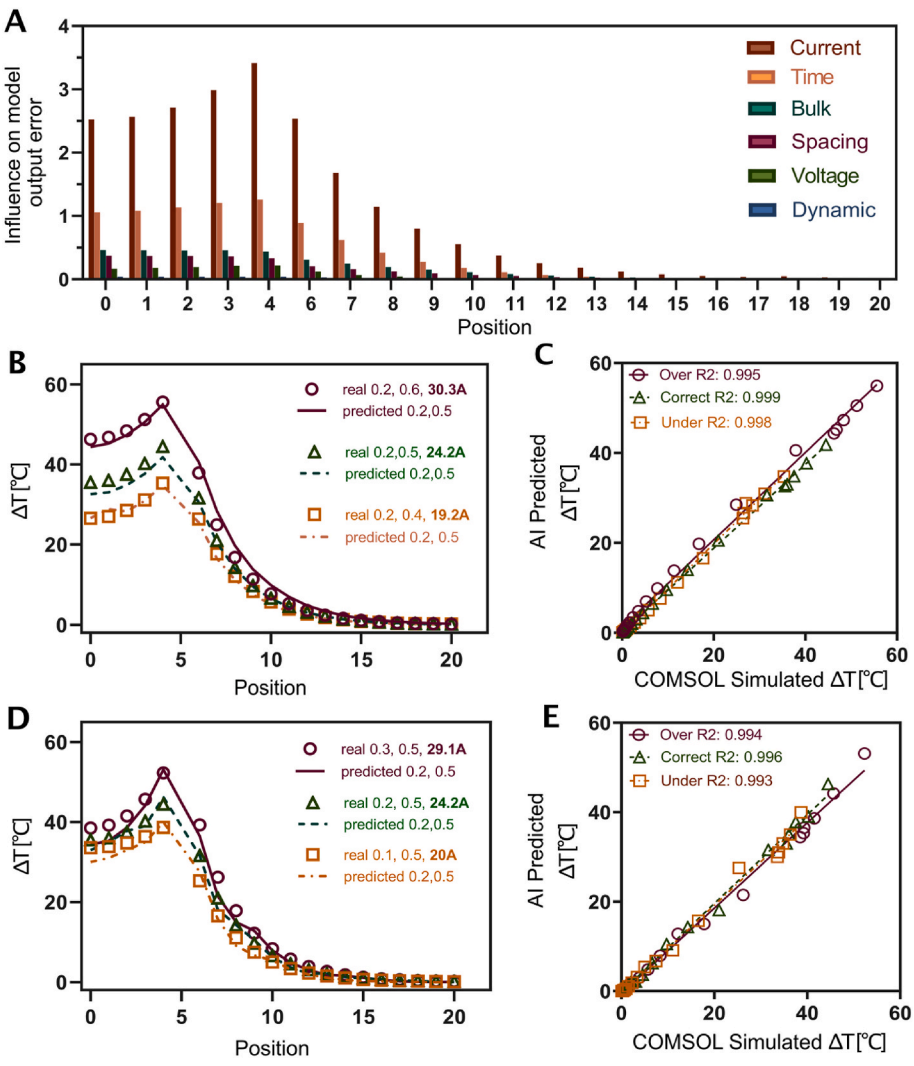

Fig. 5. Current can compensate for incorrect tissue properties. **A)** SHapley Additive exPlanations (SHAP) plot for explaining the local influence model inputs have on the output. **B)** Incorrect input measurements for the change in conductivity due to electroporation effects have no effect on model error. **C)** Linear regression for the simulated COMSOL change in temperatures versus the AI predicted change in temperature for the under, correct, and over estimations of final conductivity. **D)** Incorrect input measurements for the bulk conductivity have no effect on model error. **E)** Linear regression for the simulated COMSOL change in temperatures versus the AI predicted change in temperature for the under, correct, and over estimation of initial bulk conductivity.

than the lower temperature positions. Fig. 5 also shows that the SHAP values were largest for positions 0–10, because they were the outputs that contributed the most towards the model error.

By using SHAP for feature selection, we saw that current reading and pulse number were the two most important parameters for this model. Computational models for temperature rise are deterministic and use estimated tissue properties, pulsing parameters, and probe geometries to simulate temperature rise. Subsequently, current is calculated as an output of these simulations, but during actual treatment, the simulated current and actual current recorded are often significantly different. This discrepancy can occur through incorrect tissue estimations, which means that the prospective temperature estimations are also incorrect. Further, if the treatment differs from the one simulated (through cardiac sync or stops), the simulation of temperature rise is no longer useful.

The NN developed in this work suggests that the measured current during treatment is a more powerful predictor for temperature rise than all the other parameters chosen. Conveniently, applied current can be measured in real time, and the only parameters that may not be known with a degree of certainty are tissue properties. Since this model can accurately predict temperature rise with known parameters as inputs, even with incorrect tissue properties, we reduce the need for accurate tissue properties. Current is largely dependent on the electrical tissue properties, which allows for the the recorded parameters that we know with certainty to compensate for the estimated ones. Small errors in chosen tissue conductivity (±0.01–0.03 S/m) are within the standard deviation of characterized tissue properties [40,42] and can cause significant changes in both temperature distributions and applied current (**Supplement S1**). This effect is exaggerated further for the tumor treatments, where estimated parameters differ even more from truth. The ability of our NN to predict temperature accurately, even with incorrect *a priori* knowledge about the tissue, is important as a non-invasive monitoring method.

Some clinicians use current as an endpoint for treatment, but in many cases current does not change significantly after the first few pulses. Likewise, in liver 2, we saw the current did not increase between pulse 10 and pulse 90 (Fig. 6B). If we only used current or a change in current for temperature rise predictions without including pulse number, then the predicted temperature would not increase. Even though current is the most influential parameter, pulse number now seems to compensate for current and accurately predict the temperature rise. Pulse number is then also an important property that future iterations of this/other models should consider using, and models that solely use changes in tissue impedance might not be able to fully capture temperature rise.

While this model was able to predict well against the NanoKnife® which only had a 3 s delay every 10 pulses, all clinical applications of IRE synchronize pulsing with the cardiac cycle, which can change the rate that pulses are applied. Large changes in the duty cycle can influence thermal heating greatly. Additional parameters may be needed to incorporate changes in pulsing frequency, delays for cardiac

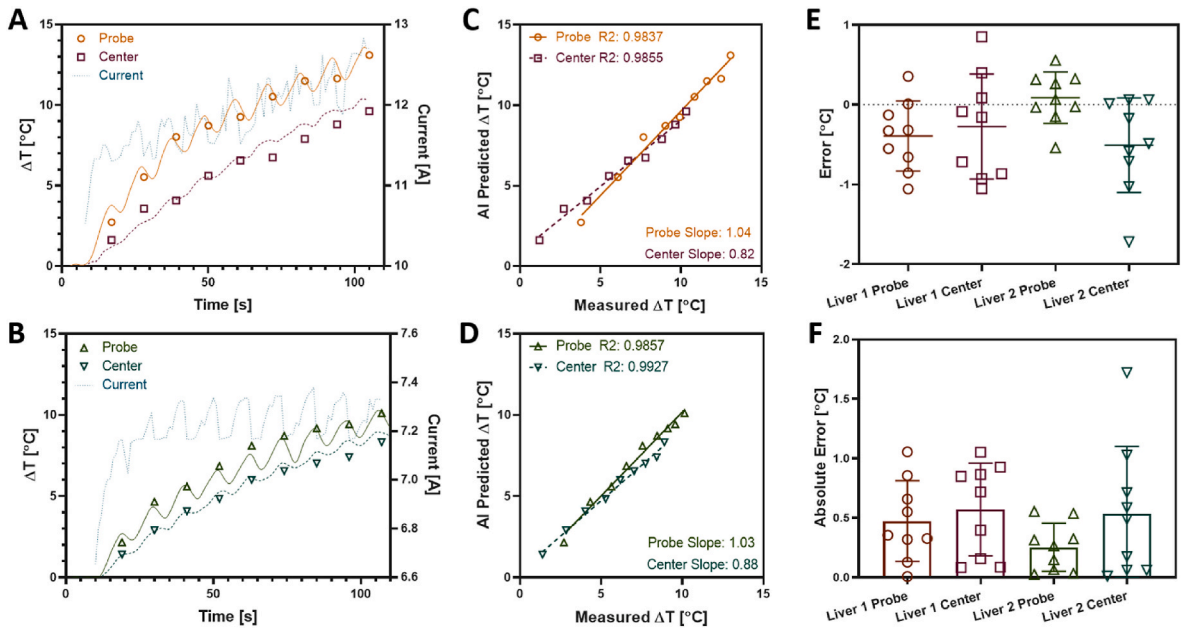

Fig. 6. Ex Vivo Perfused Liver Model. Temperature was recorded with fiber optic temperature probes at the midpoint between the two probes and at the electrode surface. **A & B)** AI predicted temperature rises and real recorded temperature rises over the course of electroporation treatment in two perfused porcine livers. **C & D)** The linear fit between the real recorded temperature and AI predicted temperatures. **E)** The error between the AI predicted temperatures and the real recorded temperature. The means and 95% confidence intervals are shown. **F)** The absolute error between the AI predicted temperature and real recorded temperature. The means and standard deviations are shown.

synchronization, or programmed delays between trains of pulses. For these models, perfusion rate of the organ becomes more significant, as there is more time for heat dissipation between gaps in pulsing. We chose one perfusion rate to limit the complexity of this study since we modeled a steady, uninterrupted 1 Hz pulse, but a parametric sweep incorporating other pulsing frequencies and perfusion rates could make the model more complete. Also, more complex time-dependent models could integrate rolling current, time, and pulse number over the entire treatment to predict the temperature distribution at the current pulse, instead of treating each pulse as a separate, isolated condition. These models may also be more robust against short term fluctuations in recorded current.

We chose to model the temperature distribution for a 2-needle set up since that is what is commonly used in clinic for IRE cancer treatments [47–49]. However, research and interests are increasing in using single insertion probes for laparoscopic IRE treatments. To develop similar temperature prediction algorithms for other geometries, a new COMSOL model would need to be generated using that specific probe geometry. The 2-needle geometry is flexible in that probe spacing and electrode exposure is incorporated in the model. For bipolar probes, there is insulation separating two electrodes on the same probe. The probe insulation length and electrode exposure would now need to be explicitly modeled and used as an input to the AI model. For a single needle with a distant grounding pad, the current must pass through many heterogenous tissues, making current readings more difficult to interpret. This might pose a problem for non-invasive temperature prediction methods where impedance is an important variable.

Further, for the purposes of this study, we used an on-time (pw) of 100 μs and a pulse period (τ) of 1 s, because they are the most common in cancer treatment protocols. The duty cycle (pw/τ) has a direct influence on Joule heating within the tissue (eq. (4)). To incorporate a different duty cycle, the AI model must either be retrained on a new dataset or incorporate the duty cycle as an input parameter. The phase of the waveform alone does not affect the Joule heating; the conductivity of the tissue is affected by frequency of the waveform, and biphasic waveforms are often higher frequencies than monophasic waveforms. With an increase in frequency, there will be a slight increase in bulk conductivity as the capacitance of the tissue is attenuated [29,50,51]. The increase in tissue conductance will be realized with an increase in applied current and, subsequently, an increase in Joule heating. The contributions due the waveform are considered with the tissue property selection and current readings.

While the only biophysical tissue property explicitly defined in the AI model is the dynamic conductivity, other tissue properties such as density, heat capacity, and thermal conductivity are present within the heat equation (eq. (4)) and influence temperature rise. However, for applications of electroporation these values do not vary significantly between prostate, pancreas, liver, brain, or kidneys (Supplemental Table S1). We chose a singular value for density, heat capacity, and thermal conductivity for all our finite element models to simplify creating the dataset. Keeping the dynamic conductivity curve constant for equal comparison, the difference from the highest temperature rise (pancreas) and lowest (brain) is <2% (average < 0.8% difference) at the highest temperature spot. Further, the linear regression between one organ and any other all have $R^2 > 0.998$ (p-value <0.00001) (Supplement S2). This suggests that we do not need to explicitly define density, heat capacity, or thermal conductivity within our AI model, significantly reducing the computational burden to produce the dataset. While it would be more accurate to incorporate every independent tissue parameter, limitations forced us to choose the most important parameters. Future iterations could include more specific tissue parameters for the organ of interest. Further, terms like density and heat capacity can be combined into single terms to reduce the parametric sweep size and improve model creation times.

This AI may also be incorporated for use with a 4-probe set up. If we consider a 4-probe set up as 4 independent pairs of 2-needle electrodes, then the AI would need to be fed values from each pair. A problem in temperature prediction could arise with temperature convection from the other 2-needle pairs dissipating into the area being predicted. The MLP predicts a change in temperature instead of absolute temperature, and heat generation is not greatly affected by slight changes in initial tissue temperature. Therefore, if the contributions to temperature rise between the two electrodes is mostly due to Joule heating and not from convection from other electrode pairs, then we expect temperature rise

predictions will still be accurate. Another problem could arise from the lower pulse rate, which this AI was not explicitly trained on. A future study incorporating tissue perfusion and average pulse frequency could be used to validate this 2-needle AI for a prediction with any number of 2-needle electrode pairs.

While these methods can be translated to other probe geometries, special consideration must be given to cardiac ablation, due to the method of electric field delivery and the complex geometry. Cardiac ablation typically employs electrodes guided into the left atrium, and these electrodes contact the atrial wall to deliver electric fields through the endocardium without penetration into the tissue itself [22,52]. Various factors that are not present for cancer ablation applications are present in cardiac ablation: uncertain atrial wall thicknesses, probe contact with the endocardium, contact angle, and proprietary/unknown pulsing parameters. Even with inconsistent contact with the atrial wall, the blood can still carry the electric field to the tissue; however, this leads to erratic and unreliable current readings. We found that current was the most important parameter for temperature prediction, so uncertain contact may lead to unreliable temperature predictions.

5. Conclusion

In this study, we have shown that an accurate and robust temperature prediction model can be developed using estimated tissue properties (bulk and dynamic conductivity), known geometric properties (probe spacing), and easily measurable treatment parameters (applied voltage, current, and pulse number). We developed the dataset on realistic 2-D COMSOL™ Multiphysics simulations with conditions encompassing most electroporation applications. Using feature contribution analysis, we found that temperature prediction is mostly dependent on current and pulse number and found that the model still predicts accurately, even when incorrectly estimated tissue properties are intentionally used for the model input parameters. Lastly, we show that the model can accurately predict temperature rise within an ex vivo perfused porcine liver, with error <0.5 °C between the predicted temperature and the real recorded temperature. This model, using easily acquired parameters, was able to predict accurate temperature rise in 1968 unique conditions with no observable outliers and can be extrapolated to conditions it has not seen through pattern recognition. Further, we believe the simple, readily available input parameters would allow this model to be easily incorporated in many already available electroporation systems.

Author contributions

Conceptualization, E.J.J. and R.V.D.; methodology, E.J.J., S.C., K.A.; formal analysis, E.J.J.; resources, R.V.D; data curation, writing, E.J.J, S.C., K.A., D.Y.; supervision, R.V.D. All authors have read and agree on the published version of the manuscript.

Data availability statement

The data that supports the findings of this study are available within the article and its supplementary material.

Summary

Irreversible electroporation (IRE) is a nonthermal focal ablation modality that employs high-magnitude (1–3 kV), short (70–100 μs) electric pulses applied directly into tissue. The applied electric field generates a transmembrane potential on cells to overcome the forces holding the phospholipid bilayer together causing irreversible necrosis and apoptosis of cells within the tissue. IRE can generate clinically relevant ablation sizes without the need for chemotherapeutics and without significant thermal heating. The nonthermal mechanism for irreversible electroporation has been paramount for treating tumors and cardiac tissue in anatomically sensitive areas, where there is concern about damage to nearby bowels, ducts, blood vessels, or nerves. However, Joule heating still occurs as a secondary effect of applying an electric field through a resistive tissue and must be minimized to maintain these benefits at high voltages. Numerous thermal mitigation protocols have been proposed to minimize temperature rise, but intraoperative temperature monitoring is still needed. Further, finite element modeling requires knowledge about the system that may vary significantly from reality; the resulting current from an applied potential may be different during treatment than is simulated, making the prospective simulations imprecise. Therefore, algorithms that can relate current read during IRE treatments to temperature generation and monitoring is greatly needed.

We show that an accurate and robust temperature prediction model can be developed using a simple multi-layer perceptron. The inputs to the model are estimated tissue properties (bulk and dynamic conductivity), known geometric properties (probe spacing), and easily measurable treatment parameters (applied voltage, current, and pulse number). We develop the AI on realistic 2-D finite element model simulations with conditions encompassing most electroporation applications. Calculating feature contributions, we found that temperature prediction is mostly dependent on current and pulse number and show that the model remains accurate when incorrect tissue properties are intentionally used for the model input parameters. Lastly, we show that the model can accurately predict temperature rise within an ex vivo perfused porcine liver, with error <0.5 °C between the predicted and measured temperatures. In cases where current does not significantly change over treatment, we show that pulse number can compensate for the current, to aide in temperature prediction.

This model, using easily acquired parameters, is shown to predict temperature rise in over 1000 unique test conditions with <1 °C error and no observable outliers. The use of neural networks can overcome the limitations of finite element models, since they can predict the temperature rise as current is being read during treatment and is not as dependent on knowing the exact tissue properties. Further, the use of simple and readily available input parameters would allow this model to be easily incorporated in many already available electroporation systems and treatment planning protocols.

Declaration of competing interest

The authors have patents related to the paper. R.V.D. has ownership interest for startup companies within the field of bioelectrics. In addition, R.V.D. also receives royalty income from technologies he has invented and serves as a consultant.

Acknowledgments and Funding

This research was funded in part by the NIH RO1 (RO1CA24047).

Appendix A. Supplementary data

Supplementary data to this article can be found online at https://doi.org/10.1016/j.compbiomed.2023.107019.

References

[1] K.N. Aycock, R.v. Davalos, Irreversible electroporation: background, theory, and review of recent developments in clinical oncology, Bioelectricity 1 (4) (Dec. 2019) 214–234, https://doi.org/10.1089/BIOE.2019.0029/ASSET/IMAGES/LARGE/BIOE.2019.0029_FIGURE7.JPEG.

[2] T. Kotnik, L. Rems, M. Tarek, D. Miklavčič, Membrane electroporation and electropermeabilization: mechanisms and models, Annu. Rev. Biophys. 48 (2019) 63–91, https://doi.org/10.1146/annurev-biophys-052118.

[3] J.C. Weaver, Y.A. Chizmadzhev, Theory of Electroporation: A Review, 1996.

[4] L. Towhidi, T. Kotnik, G. Pucihar, S.M.P. Firoozabadi, H. Mozdarani, D. Miklavčič, Variability of the minimal transmembrane voltage resulting in detectable

membrane electroporation, Electromagn. Biol. Med. 27 (4) (Dec. 2008) 372–385, https://doi.org/10.1080/15368370802394644.
[5] J. Teissié, M.P. Rols, An experimental evaluation of the critical potential difference inducing cell membrane electropermeabilization, Biophys. J. 65 (1) (1993) 409–413, https://doi.org/10.1016/S0006-3495(93)81052-X.
[6] M. Hibino, H. Itoh, K. Kinosita, Time courses of cell electroporation as revealed by submicrosecond imaging of transmembrane potential, Biophys. J. 64 (6) (1993) 1789–1800, https://doi.org/10.1016/S0006-3495(93)81550-9.
[7] L.M. Mir, S. Orlowski, J. Belehradek, C. Paoletti, Electrochemotherapy Potentiation of Antitumour Effect of Bleomycin by Local Electric Pulses, 1991.
[8] G. Sersa, B. Stabuc, M. Cemazar, B. Jancar, D. Miklavcic, Z. Rudolf, Electrochemotherapy with Cisplatin: Potentiation of Local Cisplatin Antitumour Effectiveness by Application of Electric Pulses in Cancer Patients, 1998.
[9] G. Serša, B. Stabuc, D. Miklavcic, Z. Rudolf, Electrochemotherapy with cisplatin: clinical experience in malignant melanoma patients, Clin. Cancer Res. 6 (2000) 863–867 [Online]. Available: http://aacrjournals.org/clincancerres/article-pdf/6/3/863/2076012/df030000863.pdf.
[10] E. Neumann, M. Schaefer-Ridder, Y. Wang, P.H. Hofschneider, Gene transfer into mouse lyoma cells by electroporation in high electric fields, EMBO J. 1 (7) (1982) 841–845, https://doi.org/10.1002/j.1460-2075.1982.tb01257.x.
[11] G. Chu, H. Hayakawa, P. Berg, Electroporation for the efficient transfecdon of mammalian cells with DNA, Nucleic Acids Res. 15 (1987) [Online]. Available: https://academic.oup.com/nar/article/15/3/1311/1166855. (Accessed 6 December 2022).
[12] J.F. Edd, L. Horowitz, R.v. Davalos, L.M. Mir, B. Rubinsky, In vivo results of a new focal tissue ablation technique: irreversible electroporation, IEEE Trans. Biomed. Eng. 53 (7) (Jul. 2006) 1409–1415, https://doi.org/10.1109/TBME.2006.873745.
[13] R. v Davalos, L.M. Mir, B. Rubinsky, Tissue ablation with irreversible electroporation, Ann. Biomed. Eng. 33 (2) (2005) 223–231, https://doi.org/10.1007/s10439-005-8981-8.
[14] B. Al-Sakere, et al., Tumor ablation with irreversible electroporation, PLoS One 2 (11) (Nov. 2007), https://doi.org/10.1371/JOURNAL.PONE.0001135.
[15] D. Stillström, M. Beermann, J. Engstrand, J. Freedman, H. Nilsson, Initial experience with irreversible electroporation of liver tumours, Eur. J. Radiol. Open 6 (Jan. 2019) 62–67, https://doi.org/10.1016/J.EJRO.2019.01.004.
[16] N. Kalra, et al., Irreversible electroporation for unresectable hepatocellular carcinoma: initial experience, Cardiovasc. Intervent. Radiol. 42 (2019), https://doi.org/10.1007/s00270-019-02164-2.
[17] W. Cheung, H. Kavnoudias, S. Roberts, B. Szkandera, W. Kemp, K.R. Thomson, Irreversible electroporation for unresectable hepatocellular carcinoma: initial experience and review of safety and outcomes, Technol. Cancer Res. Treat. 12 (3) (2013) 233–241, https://doi.org/10.7785/tcrt.2012.500317.
[18] B.M. Benway, Irreversible electroporation of renal cell carcinoma: a first-in-man phase I clinical study, Year Bk. Urol. 2011 (Jan. 2011) 36–37, https://doi.org/10.1016/j.yuro.2011.06.061.
[19] E. Guenther, et al., Prostate cancer treatment with Irreversible Electroporation (IRE): safety, efficacy and clinical experience in 471 treatments, PLoS One 14 (4) (Apr. 2019), https://doi.org/10.1371/journal.pone.0215093.
[20] F. Collettini, et al., Image-guided irreversible electroporation of localized prostate cancer: functional and oncologic outcomes, Radiology 292 (1) (2019) 250–257, https://doi.org/10.1148/radiol.2019181987.
[21] R. Martin II, K. Mcfarland, S. Ellis, V. Velanovich, Irreversible electroporation in locally advanced pancreatic cancer: potential improved overall survival, Ann. Surg Oncol. 20 (2013), https://doi.org/10.1245/s10434-012-2736-1.
[22] A. Sugrue, et al., Irreversible electroporation for the treatment of cardiac arrhythmias, 5, in: Expert Review of Cardiovascular Therapy, vol. 16Taylor and Francis Ltd, 2018, pp. 349–360, https://doi.org/10.1080/14779072.2018.1459185. May 04.
[23] I. Sorokin, N. Canvasser, B. Johnson, E. Lucas, J.A. Cadeddu, Irreversible electroporation for renal ablation does not cause significant injury to adjacent ureter or bowel in a porcine model, J. Endourol. 35 (6) (Jun. 2021) 873–877, https://doi.org/10.1089/END.2020.0856/ASSET/IMAGES/LARGE/END.2020.0856_FIGURE6.JPEG.
[24] E. Ueshima, et al., Transmural ablation of the normal porcine common bile duct with catheter-directed irreversible electroporation is feasible and does not impact duct patency, Gastrointest. Endosc. 87 (1) (2018), https://doi.org/10.1016/j.gie.2017.05.004.
[25] E. Maor, A. Ivorra, J. Leor, B. Rubinsky, The effect of irreversible electroporation on blood vessels, Technol. Cancer Res. Treat. 6 (4) (2007) 307–312 [Online]. Available: www.tcrt.org [Online]. Available:.
[26] W. Li, Q. Fan, Z. Ji, X. Qiu, Z. Li, The effects of irreversible electroporation (IRE) on nerves, PLoS One 6 (4) (2011), https://doi.org/10.1371/journal.pone.0018831.
[27] P. Philips, D. Hays, R.C.G. Martin, Irreversible Electroporation Ablation (IRE) of Unresectable Soft Tissue Tumors: Learning Curve Evaluation in the First 150 Patients Treated, 2013, https://doi.org/10.1371/journal.pone.0076260.
[28] J. Rudno-Rudzí Nska, W. Kielan, M. Guzí Nski, M. Płochocki, and J. Kulbacka, "The First Study of Irreversible Electroporation with Calcium Ions and Chemotherapy in Patients with Locally Advanced Pancreatic Adenocarcinoma", doi: 10.3390/app10155163.
[29] P. Agnass, et al., Mathematical modeling of the thermal effects of irreversible electroporation for in vitro, in vivo, and clinical use: a systematic review, Int. J. Hyperther. 37 (1) (2020) 486–505, https://doi.org/10.1080/02656736.2020.1753828.
[30] P.A. Garcia, J.H. Rossmeisl Jr., R.E. Neal II, T.L. Ellis, R. V Davalos, A Parametric Study Delineating Irreversible Electroporation from Thermal Damage Based on a Minimally Invasive Intracranial Procedure, 2011, https://doi.org/10.1186/1475-925X-10-34.
[31] T.J. O'Brien, et al., Effects of Internal Electrode Cooling on Irreversible Electroporation Using a Perfused Organ Model, vol. 35, Jan. 2018, pp. 44–55, https://doi.org/10.1080/02656736.2018.1473893, 1.
[32] C.B. Arena, R.L. Mahajan, M. Nichole Rylander, R.v. Davalos, An experimental and numerical investigation of phase change electrodes for therapeutic irreversible electroporation, J. Biomech. Eng. 135 (11) (Nov. 2013), https://doi.org/10.1115/1.4025334/370890.
[33] T.J. O'Brien, et al., Cycled pulsing to mitigate thermal damage for multi-electrode irreversible electroporation therapy, Int. J. Hyperther. 36 (1) (Jan. 2019) 953–963, https://doi.org/10.1080/02656736.2019.1657187.
[34] P. Agnass, et al., Mathematical modeling of the thermal effects of irreversible electroporation for in vitro, in vivo, and clinical use: a systematic review, Int. J. Hyperther. 37 (1) (Jan. 2020) 486–505, https://doi.org/10.1080/02656736.2020.1753828.
[35] H. Cindrič, et al., Retrospective study for validation and improvement of numerical treatment planning of irreversible electroporation ablation for treatment of liver tumors, IEEE Trans. Biomed. Eng. 68 (12) (2021), https://doi.org/10.1109/TBME.2021.3075772.
[36] M.F. Lorenzo, S.P. Bhonsle, C.B. Arena, R.V. Davalos, Rapid impedance spectroscopy for monitoring tissue impedance, temperature, and treatment outcome during electroporation-based therapies, IEEE Trans. Biomed. Eng. 68 (5) (2021), https://doi.org/10.1109/TBME.2020.3036535.
[37] S.N. Campelo, E.J. Jacobs, K.N. Aycock, R.V. Davalos, Real-time temperature rise estimation during irreversible electroporation treatment through state-space modeling, Bioengineering 9 (10) (2022), https://doi.org/10.3390/BIOENGINEERING9100499.
[38] S. Corovic, I. Lackovic, P. Sustaric, T. Sustar, T. Rodic, D. Miklavcic, Modeling of electric field distribution in tissues during electroporation, Biomed. Eng. Online 12 (1) (Feb. 2013), https://doi.org/10.1186/1475-925X-12-16.
[39] K.N. Rai, S.K. Rai, Effect of metabolic heat generation and blood perfusion on the heat transfer in the tissues with a blood vessel, Heat Mass Tran. 35 (1999).
[40] N. Beitel-White, et al., Multi-tissue analysis on the impact of electroporation on electrical and thermal properties, IEEE Trans. Biomed. Eng. 68 (3) (2021) 771–782, https://doi.org/10.1109/TBME.2020.3013572.
[41] C. Rossmann, D. Haemmerich, Review of temperature dependence of thermal properties, dielectric properties, and perfusion of biological tissues at hyperthermic and ablation temperatures, Crit. Rev. Biomed. Eng. 42 (6) (2014).
[42] IT'IS Database for thermal and electromagnetic parameters of biological tissues, Version 4.0. https://itis.swiss/virtual-population/tissue-properties/downloads/database-v4-1/. (Accessed 15 August 2022).
[43] S. Bhonsle, et al., Characterization of irreversible electroporation ablation with a validated perfused organ model, J. Vasc. Intervent. Radiol. 27 (12) (Dec. 2016) 1913–1922.e2, https://doi.org/10.1016/J.JVIR.2016.07.012.
[44] S. Lipovetsky, M. Conklin, Analysis of regression in game theory approach, Appl. Stoch Model Bus. Ind. 17 (4) (Oct. 2001) 319–330, https://doi.org/10.1002/ASMB.446.
[45] E. Štrumbelj, I. Kononenko, Explaining prediction models and individual predictions with feature contributions, Knowl. Inf. Syst. 41 (3) (Nov. 2014) 647–665, https://doi.org/10.1007/s10115-013-0679-x.
[46] M.T. Ribeiro, S. Singh, C. Guestrin, Why should I trust you?': explaining the predictions of any classifier, in: NAACL-HLT 2016 - 2016 Conference of the North American Chapter of the Association for Computational Linguistics: Human Language Technologies, Proceedings of the Demonstrations Session, Feb. 2016, pp. 97–101, https://doi.org/10.48550/arxiv.1602.04938.
[47] H.J. Scheffer, et al., Ablation of Locally Advanced Pancreatic Cancer with Percutaneous Irreversible Electroporation: Results of the Phase I/II PANFIRE Study, vol. 282, Sep. 2016, pp. 585–597, https://doi.org/10.1148/radiol.2016152835, 2.
[48] A. Eller et al., "Local Control of Perivascular Malignant Liver Lesions Using Percutaneous Irreversible Electroporation: Initial Experiences", doi: 10.1007/s00270-014-0898-x.
[49] G. Narayanan, et al., Percutaneous image-guided irreversible electroporation for the treatment of unresectable, locally advanced pancreatic adenocarcinoma, J. Vasc. Intervent. Radiol. 28 (3) (Mar. 2017) 342–348, https://doi.org/10.1016/J.JVIR.2016.10.023.
[50] S. Bhonsle, M.F. Lorenzo, A. Safaai-Jazi, R.V. Davalos, Characterization of nonlinearity and dispersion in tissue impedance during high-frequency electroporation, IEEE Trans. Biomed. Eng. 65 (10) (2018) 2190–2201, Oct, https://doi.org/10.1109/TBME.2017.2787038.
[51] C. Gabriel, A. Peyman, E.H. Grant, Electrical conductivity of tissue at frequencies below 1 MHz, Med. Biol. Phys. Med. Biol. 54 (2009) 4863–4878, https://doi.org/10.1088/0031-9155/54/16/002.
[52] F.H.M. Wittkampf, R. van Es, K. Neven, Electroporation and its relevance for cardiac catheter ablation, JACC Clin. Electrophysiol. 4 (8) (Aug. 2018) 977–986, https://doi.org/10.1016/J.JACEP.2018.06.005.